PHYSICAL REVIEW B **95**, 220410(R) (2017)

Nanoscale thermoelectrical detection of magnetic domain wall propagation

Patryk Krzysteczko,[1,2] James Wells,[2,3] Alexander Fernández Scarioni,[1] Zbynek Soban,[4] Tomas Janda,[4,5] Xiukun Hu,[1] Vit Saidl,[5,4] Richard P. Campion,[6] Rhodri Mansell,[7] Ji-Hyun Lee,[7] Russell P. Cowburn,[7] Petr Nemec,[5] Olga Kazakova,[3] Joerg Wunderlich,[4,8] and Hans Werner Schumacher[1]

[1]*Physikalisch-Technische Bundesanstalt, Bundesallee 100, 38116 Braunschweig, Germany*
[2]*Physikalisch-Technische Bundesanstalt, Abbestr. 2-12, 10587 Berlin, Germany*
[3]*National Physical Laboratory, Teddington TW11 0LW, United Kingdom*
[4]*Institute of Physics, Academy of Science of the Czech Republic, Cukrovarnická 10, 162 00 Prague 6, Czech Republic*
[5]*Faculty of Mathematics and Physics, Charles University, Ke Karlovu 3, 121 16 Prague 2, Czech Republic*
[6]*School of Physics and Astronomy, University of Nottingham, Nottingham NG7 2RD, United Kingdom*
[7]*Thin Film Magnetism Group, Cavendish Laboratory, University of Cambridge, JJ Thomson Avenue, Cambridge CB3 0HE, United Kingdom*
[8]*Hitachi Cambridge Laboratory, Cambridge CB3 0HE, United Kingdom*

(Received 20 March 2017; published 27 June 2017)

In magnetic nanowires with perpendicular magnetic anisotropy (PMA) magnetic domain walls (DWs) are narrow and can move rapidly driven by current induced torques. This enables important applications like high-density memories for which the precise detection of the position and motion of a propagating DW is of utmost interest. Today's DW detection tools are often limited in resolution, require complex instrumentation, or can only be applied on specific materials. Here we show that the anomalous Nernst effect provides a simple and powerful tool to precisely track the position and motion of a single DW propagating in a PMA nanowire. We detect field and current driven DW propagation in both metallic heterostructures and dilute magnetic semiconductors over a broad temperature range. The demonstrated spatial accuracy below 20 nm is comparable to the DW width in typical metallic PMA systems.

DOI: 10.1103/PhysRevB.95.220410

Recent concepts for high-density memory, logic, and sensor devices [1] rely on the controlled positioning and propagation of narrow magnetic domain walls (DWs) [2] in nanowires with perpendicular magnetic anisotropy (PMA) [3–7]. To study and develop such systems requires a reliable high-resolution tool for detecting the DW position inside the wire. While magneto-optical microscopy is limited in spatial resolution [3,8], high-resolution imaging such as spin resolved electron microscopy [9], nanomagnetometry [10], or magnetic force microscopy (MFM) [11] can be complex, time consuming, and invasive. The anomalous Hall effect (AHE) allows one to probe the position and motion of a DW inside a PMA Hall cross with nanometer resolution [12–15], but the DW position outside of the Hall cross is not accessible. Other electrical measurements like giant magnetoresistance detection can only be applied on specific spin valve nanowires [16,17]. Over recent years, the field of spin caloritronics [18] has explored the interplay of heat and spin currents in spintronic materials and devices. With respect to DW devices, thermal spin transfer torque [19,20], thermally driven DW motion [21–23], and the magneto Seebeck contribution of an individual DW [24] were studied. At the same time, the anomalous Nernst effect (ANE) moved into focus from being part of a careful analysis of spin-caloritronic measurements [25–28] to detection of magnetization reversal [29,30] and magnetization dynamics [31,32] in magnetic thin films.

Here, we show that ANE provides a powerful tool to probe DW propagation in magnetic nanowires with nanoscale accuracy. Using a simple thermoelectrical measurement setup we detect current induced, magnetic field induced, and MFM induced DW propagation as well as DW depinning from individual nanoscale pinning sites. To highlight the generic character of this method, we apply it on two distinct ferromagnetic PMA systems, namely, metallic Pt/CoFeB/Pt wires with high Curie temperature T_C and wires patterned from a (GaMn)(AsP) magnetic semiconductor film [8] with T_C below room temperature. We demonstrate DW position detection with spatial accuracy down to 20 nm comparable to the DW width in typical PMA materials with potential for further improvement.

As sketched in Fig. 1(a), AHE has been used to detect DW propagation within PMA Hall crosses. The AHE voltage V_{AHE} is proportional to the average out-of-plane magnetization in the cross area which depends on the DW position. However, an AHE signal is only generated within the cross region where the probe current I is applied. By instead using *thermo*electrical measurements of the ANE (in analogy to the *electrical* AHE) the sensitive region can be extended over the whole wire length as shown in Fig. 1(b). To do so, a transverse in-plane thermal gradient ∇T_y is created by a heater line parallel to the wire. ∇T_y is perpendicular to the PMA magnetization $M^{\downarrow,\uparrow}$ thus resulting in an ANE voltage V_{ANE} between the wire ends. For fully saturated magnetization of the complete wire the ANE voltage is given by

$$V_{ANE}^{max} = -N_{ANE}\mu_0 m_z l \overline{\nabla T_y}. \quad (1)$$

Here N_{ANE} is the ANE coefficient per magnetic moment, μ_0 is the vacuum permeability, m_z is the z component of the magnetization (with $m_z = \pm M_S$ the saturation magnetization), l is the wire length, and $\overline{\nabla T_y}$ is the average of ∇T_y over the wire length. A single DW at position x_{DW} inside the wire divides the magnetization distribution into two domains with opposite perpendicular magnetization $m_z{}^{\downarrow} = -m_z{}^{\uparrow}$. If the DW is positioned in the center of the wire (defined $x_{DW} = 0$) the ANE contributions of the two domains compensate and $V_{ANE}(x_{DW} = 0)$ vanishes. DW motion changes the ratio

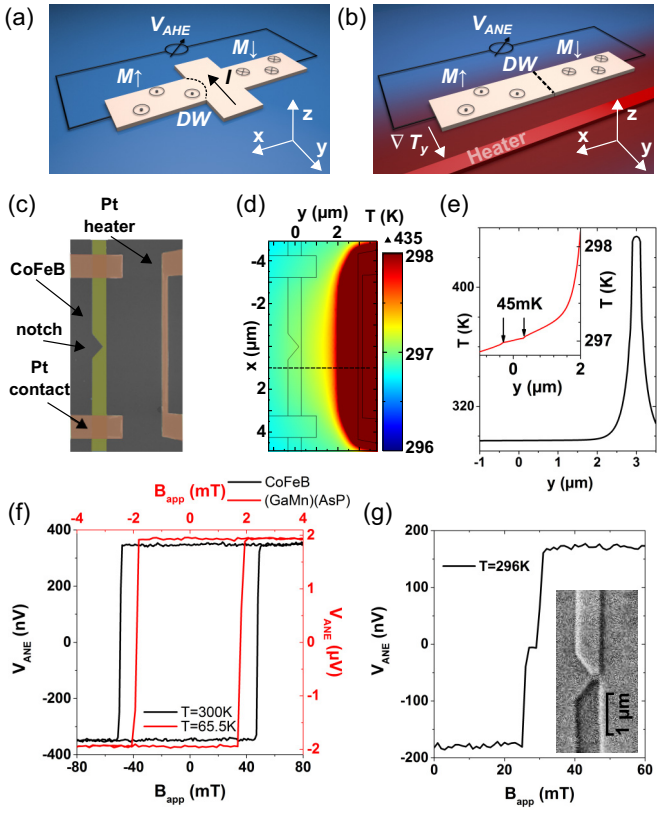

FIG. 1. Principle of ANE-based DW detection: (a) AHE DW detection by probe current I inside a Hall cross. (b) ANE DW detection in a PMA wire: a transverse temperature gradient ∇T_y generates an ANE voltage V_{ANE} along the wire depending on x_{DW}. (c) False color electron micrograph of CoFeB nanowire (green) with Pt contacts and heater line (brown). The wire l length between the contacts is 6.4 μm. The wire is 600 nm wide. A 200-nm-wide notch is situated at the center. (d) Color map of the simulated temperature distribution for electrical heating with $P_{heat} = 5.1$ mW. (e) The temperature profile along the dashed line in the simulation. The temperature drops from 435 K at the heater to 297 K at the CoFeB wire where an edge-to-edge temperature drop of 45 mK is calculated (marked in the inset by arrows). (f) ANE reversal loops from full negative to positive saturation. V_{ANE} is plotted vs B_{app}. The black curve shows data of a CoFeB wire at room temperature and $P_{heat} = 7.4$ mW. The red curve shows (GaMn)(AsP) data taken at $T = 65.5$ K and $P_{heat} = 0.75$ mW. (g) Pinning of a propagating DW at the notch of a CoFeB device. V_{ANE} at $P_{heat} = 5.1$ mW plotted as a function of B_{app} for a sweep from −200 mT to positive fields at a sweep rate of 8.3 mT/s. The plateau at $V_{ANE} = 0$ results from pinning of a propagating DW at the notch. Inset: MFM image of a pinned DW at the notch. The two contrasts correspond to opposite m_z on either side of the notch.

between the two ANE contributions and hence V_{ANE}. For a constant ∇T_y over the wire length $V_{ANE}(x_{DW})$ depends linearly on x_{DW}, thus allowing direct thermoelectrical detection of the DW position with nanoscale accuracy using

$$x_{DW} = -\frac{V_{ANE}(x_{DW})}{2N_{ANE}\mu_0 M_S \nabla T_y}. \quad (2)$$

Note that the assumption of constant $\nabla T_y(x)$ is only valid for constant wire width and for samples with a heater line longer than the wire. A more general expression of $V_{ANE}(x_{DW})$ for spatially varying $\nabla T_y(x)$ is derived in Supplemental Material [33].

Figure 1(c) shows a false color electron microscope image of a Pt/CoFeB (0.6 nm)/Pt nanowire (green) with an adjacent Pt heater line (brown). Figure 1(d) shows the simulated temperature distribution upon application of $P_{heat} = 5.1$ mW to the heater line. For details on simulations and temperature calibrations see Supplemental Material. From the temperature profile in Fig. 1(e) taken along the dashed line in Fig. 1(d) we estimate a temperature drop of 45 mK across the wire. Furthermore, the simulation yields $\overline{\nabla T_y} = 67 \pm 7$ mK/μm over the whole wire length. Figure 1(f) shows typical ANE data of magnetization reversal in out-of-plane fields for Pt/CoFeB/Pt (black) and (GaMn)(AsP) (red) devices. The metallic wire is measured at room temperature, whereas the semiconducting wire is measured at $T = 65.5$ K. Both wires show a clear hysteretic behavior in V_{ANE} with the square loop indicating magnetization reversal by fast DW motion. For both samples, V_{ANE} scales linearly with the applied heater power and hence with ∇T_y, as expected for a thermoelectrical signal (not shown). For CoFeB we obtain $V_{ANE}^{max} = 350$ nV at the given heater parameters. Using Eq. (1) with $\mu_0 M_S = 1.3$ T we estimate a room temperature ANE coefficient of $-0.37\,\mu$V(KT)$^{-1}$. For (GaMn)(AsP) we find $V_{ANE}^{max} = 2\,\mu$V and using $\mu_0 M_S = 22.9$ mT an ANE coefficient of $-1.49\,\mu$V(KT)$^{-1}$ at 65.5 K.

We will now focus on ANE-based DW detection in CoFeB devices at room temperature. Figure 1(g) shows an ANE reversal curve of a nominally identical device as characterized in Fig. 1(f). However, in this device the DW nucleation occurs at a lower field. As shown in Fig. 1(c) the wire contains a notch in the center (at $x = 0$). It can act as a pinning site for a propagating DW provided that the depinning field threshold is higher than the field threshold for nucleating a reversed domain at the end of the wire. The MFM image in the inset shows a DW pinned at the notch of the same device. For the reversal curve the sample was first saturated by an applied negative field of $B_{app} = -200$ mT. Then the field was swept to positive fields and V_{ANE} was recorded. For negative saturation, V_{ANE} remains constant at about −175 nV. At a field of ∼25 mT, V_{ANE} sharply rises to a nearly zero value. Here, a reversed domain has first nucleated at the narrow end of the nanowire [34] and then propagated to the notch where it remained pinned. As the notch is centered between the two contacts $V_{ANE}(x_{DW} = 0)$ vanishes as discussed above. Around 30 mT the DW depins from the notch and continues propagation through the remaining part of the wire, completing the magnetization reversal ($V_{ANE} = +175$ nV). The steep transitions indicate rapid DW propagation, with a propagation field threshold well below the applied field.

For a more detailed investigation, we use the local stray field B_{tip} of an MFM tip to control the DW position in CoFeB devices on the nanometer scale. As sketched in Fig. 2(a) a high moment MFM probe [33] is scanned across the wire as schematically indicated by the red line. During the scan, B_{tip} nucleates a reversed domain and displaces the DW along the wire thereby changing the ANE response as shown in Fig. 2(b). Here, V_{ANE} is plotted as a function of tip position x_{tip} for $B_{app} = 0$ mT. The right scale shows x_{DW} derived from

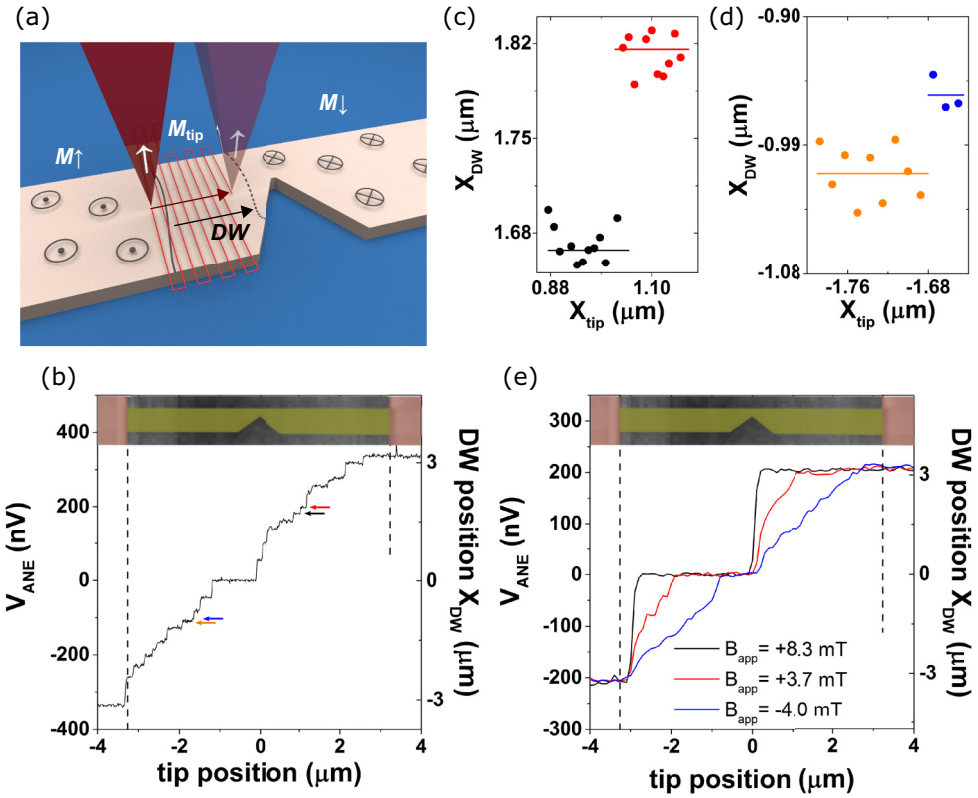

FIG. 2. ANE detection of MFM controlled DW propagation in a CoFeB nanowire. (a) Scheme of MFM controlled DW propagation as an MFM tip is scanned across the wire. The stray field of the magnetic MFM tip nucleates a reversed domain and propagates the DW ahead of the tip. (b) ANE measurement of tip induced DW propagation at $B_{\mathrm{app}} = 0, P_{\mathrm{heat}} = 7.3\,\mathrm{mW}$, and MFM tip x velocity of 25 nm/s. Top panel shows wire geometry relative to tip position. Plateaus indicate stepwise DW motion between pinning sites. The wide plateau near the center corresponds to pinning at the notch. (c) and (d) Details of plateaus indicated by arrows in (b) plotted with corresponding colors for data and arrows. (e) ANE measurement of tip induced DW propagation at applied fields of $B_{\mathrm{app}} = -4.0\,\mathrm{mT}$ (blue), 3.7 mT (red), and 8.3 mT (black). $P_{\mathrm{heat}} = 5.1\,\mathrm{mW}$. Tip x velocity $= 30\,\mathrm{nm/s}$. For higher fields parallel to the tip field the DW propagates ahead of the tip. For $B_{\mathrm{app}} = 8.3\,\mathrm{mT}$ pinning only occurs at the notch.

V_{ANE}. The wire geometry relative to x_{tip} is indicated by the top image. Before the scan, the sample is saturated in negative field $B_{\mathrm{app}} = -100\,\mathrm{mT}$ and $V_{\mathrm{ANE}} = -336\,\mathrm{nV}$. The scan starts outside the first electrical contact ($x_{\mathrm{tip}} \leqslant -3.23\,\mu\mathrm{m}$) and thus outside the sensitive region of ANE measurements and V_{ANE} remains constant. Once the probe has crossed the first contact ($x_{\mathrm{tip}} = -3.23\,\mu\mathrm{m}$), an increase of V_{ANE} is observed. The small plateaus separated by sharp transitions indicate stepwise DW motion from one local energy minimum (pinning site) to the next. The energy minima are due to local fluctuations of the magnetic properties, e.g., from edge roughness, local defects, or local thickness variation of the film. The widest plateau, and hence the strongest DW pinning, is observed at the notch ($x_{\mathrm{tip}} = 0, V_{\mathrm{ANE}} = 0$). Upon entering the tapered region, the DW can reduce its length, and thus self-energy, by moving ahead of the MFM tip toward the narrowest part of the notch. After depinning from the notch, DW propagation again reveals several pinning and depinning events indicated by small plateaus before the DW exits the measurement region at the second contact ($x_{\mathrm{tip}} = +3.23\mu\mathrm{m}$).

Figure 2(c) shows details of plateaus marked by the red and black arrows in Fig. 2(b). The position of the DW is given by $x_{\mathrm{DW}} = 9.61\frac{\mathrm{m}}{\mathrm{V}} \times V_{\mathrm{ANE}}$ with the proportionality factor calculated from $l = 6.46\,\mu\mathrm{m}$ and $2V_{\mathrm{ANE}}^{\mathrm{max}} = 672\,\mathrm{nV}$. Statistical analysis of the two plateaus in Fig. 2(c) yields absolute DW positions of $x_{\mathrm{DW}} = (1667 \pm 18)\,\mathrm{nm}$ and $x_{\mathrm{DW}} = (1816 \pm 19)\,\mathrm{nm}$. The low positioning uncertainty below 20 nm clearly demonstrates the potential of ANE-based DW detection. Estimating the DW width by $w_{\mathrm{DW}} = \pi\sqrt{AK_{\mathrm{eff}}^{-1}}$ [35] with the exchange stiffness $A = 2.5 \times 10^{-11}\,\mathrm{J\,m^{-1}}$ and the effective anisotropy $K_{\mathrm{eff}} = 5 \times 10^5\,\mathrm{J\ m^{-3}}$ yields $w_{\mathrm{DW}} \cong 20\,\mathrm{nm}$. The obtained spatial accuracy thus matches the most relevant physical length scale in our system. Taking into account the time constant and roll-off settings at the lock-in amplifier the rms noise level can be approximated by $65\ \mathrm{nm}/\sqrt{\mathrm{Hz}}$. Figure 2(d) shows the two closest plateaus of the measurement that are clearly separated within the noise level [blue and orange arrows in Fig. 2(b)]. The data yields a spatial separation of the two pinning sites of only (64 ± 30) nm demonstrating the capability of detecting depinning processes from individual pinning sites on the nanometer scale.

In Fig. 2(e) we investigate the effect of nonzero B_{app} on tip induced DW motion. Here, three curves at $B_{\mathrm{app}} = -4.0\,\mathrm{mT}$ (blue), 3.7 mT (red), and 8.3 mT (black) are shown. Note that the curves were taken at different experimental parameters (higher MFM tip velocity, lower P_{heat}) leading to a different signal-to-noise ratio than in Figs. 2(b)–2(d). The effect of

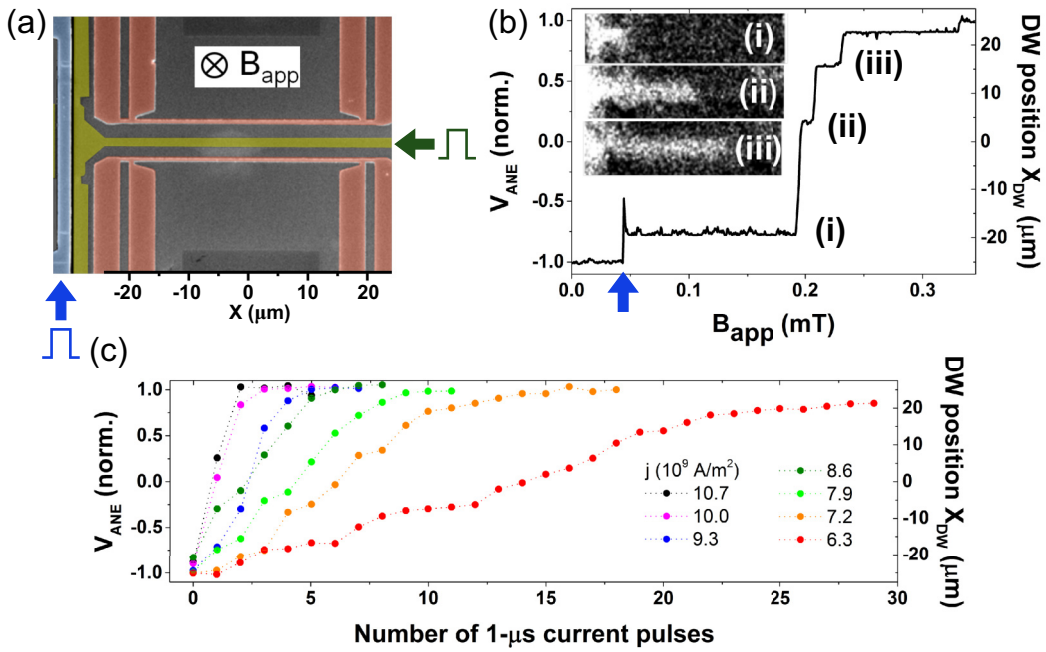

FIG. 3. ANE DW detection in a (GaMn)(AsP) microwire. (a) False color electron micrograph of the device with microwire colored in green, Pt heater line in brown, and Au nucleation strip line in blue. (b) ANE measurement during field induced DW propagation. Normalized V_{ANE} vs B_{app} at $P_{heat} = 0.5$ mW and sweep rate of 0.25 mT/s. At $B_{app} \cong 0.05$ mT a DW is nucleated (blue arrow). Plateaus result from pinning at intrinsic unintentional pinning sites. Inset: MOKE microscope images corresponding to the three pinned DW states marked (i)–(iii). (c) ANE measurement of spin torque induced DW propagation at $B_{app} = 0$. ANE data is taken after application of 1 μs pulses of current density j as indicated. For high current density high DW velocities up to 30 m/s are found. For lower current density DW propagation is hindered by pinning at various nonintentional pinning sites.

B_{app} is clearly observed. $B_{app} = -4$ mT is antiparallel to the local stray field underneath the tip ($B_{tip} > 0$). Still the remaining total field under the MFM tip $B_{tot} = B_{tip} + B_{app}$ is sufficient to propagate a reversed DW leading to a basically linear displacement of x_{DW} with x_{tip} outside the notch region. Contrarily, if the probe field coincides with the direction of B_{app} (red, black), the total field increases and the DW propagates ahead of the tip, resulting in steeper curves and less pronounced pinning inside the wire. For $B_{app} = 8.3$ mT (black), pinning inside the wire becomes negligible and DW propagation is only hindered by pinning at the notch.

With respect to Fig. 3, we now discuss thermoelectrical DW detection of field and current driven DW propagation in a 2-μm-wide and 50-μm-long (GaMn)(AsP) wire. Figure 3(a) shows the device in false colors. It contains a freestanding nucleation strip line (blue) crossing the left contact area of the magnetic wire (green). Application of a 10-ms-long nucleation pulse of 20 mA to the strip line generates an Oersted field which forms a reversed magnetized domain with a single DW present on the left-hand side of the magnetic wire.

Figure 3(b) shows the variation of the normalized ANE signal (V_{ANE} normalized by V_{ANE}^{max}) when the DW creeps along the magnetic wire driven by a small magnetic field. First, the wire is saturated in a negative saturation field of −20 mT before the field is swept at 0.25 mT/s from zero to +0.5 mT. The DW is nucleated at $B_{app} \cong 0.05$ mT (blue arrow) and the subsequent wide V_{ANE} plateau indicates DW pinning at a nonintentional pinning site until B_{app} exceeds 0.2 mT. Note that the peak at the beginning of the plateau is induced by electrical cross talk from the nucleation pulse. With increasing field, additional plateaus are observed which indicate further DW pinning during the DW propagation along the bar. The normalized ANE signal of plateaus (i)–(iii) correspond to DW positions at $x_{DW} = -20$, +4, and +15 μm. This pinning scenario is confirmed by magneto-optical Kerr effect (MOKE) micrographs of the pinned DW states shown in the insets (i)–(iii) of Fig. 3(b).

Figure 3(c) shows ANE detection of current pulse driven DW propagation at $B_{app} = 0$ mT [8]. In our experiments, 1-μs-long pulses of current densities ranging from $j = 6.3$–10.7×10^9 A/m^2 are applied. Before each series of pulses of constant current amplitude, the wire magnetization is saturated and a single DW is nucleated. The first V_{ANE} data point is measured directly after nucleation and subsequent data points are taken after each individual current pulse. At positive current, the ANE signal changes from negative to positive saturation indicating DW propagation along the wire from left to right. In contrast, spin torque current pulses of opposite polarity move the DW backwards [33]. At high current densities $j > 10 \times 10^9$ A/m^2 only few pulses are sufficient to propagate the DW through the entire wire. From the measured change of x_{DW} during a 1 μs pulse one can directly derive the DW velocity up to 30 m/s. In contrast, at low current densities $j < 9 \times 10^9$ A/m^2 many consecutive pulses are required to propagate the DW along the entire wire. Note that at lower current densities spin torque driven DW propagation is again affected by pinning. V_{ANE} thus shows pinning plateaus and does not increase linearly with the number of pulses. This

again underlines the importance of high-resolution tools for studies of current driven DW propagation as provided by ANE detection. Only with easily accessible high-resolution tools at hand, local pinning at defects can be pinpointed and a detailed understanding of the DW propagation mechanism is possible.

In summary, we have demonstrated DW position detection based solely on a simple thermopower measurement. We obtain a spatial accuracy below 20 nm for a Pt/CoFeB/Pt nanowire with PMA. This accuracy is comparable with high-resolution imaging techniques such as ambient MFM. Note that our ANE detection method can be considered as noninvasive since the applied temperature gradient is acting transversal to the direction of DW movement which should not affect its position [21]. The total temperature increase is only in the range of a few Kelvin. No high currents, like in magnetoresistance-based detection, or local fields, like in MFM, are applied to the magnetic wire. Better signal-to-noise ratios and thus higher accuracy of ANE detection should be obtainable by optimization of the sample layout. Decreasing the wire-heater separation could allow one to increase ∇T_y and hence the spatial accuracy by about 25% with only a moderate increase of the overall wire temperature. Further improvement of the sample design, e.g., by using membrane substrates, could significantly increase ∇T_y, and could enable spatial accuracy down to the few nanometer range.

This work was cofunded by EU and EMRP within JRP EXL04 SpinCal. H.W.S. acknowledges funding by DFG SPP 1538 SpinCaT. J.W. acknowledges funding from the European Research Council (ERC) Synergy Grant No. 610115. T.J., V.S., and P.N. acknowledge funding by the Grant Agency of the Czech Republic under Grant No. 14-37427G and by the Grant Agency of Charles University under Grant No. 1582417. O.K. acknowledges support by the UK government's Department for Business, Energy and Industrial Strategy. We thank André Müller for preparation of the 3D graphics.

[1] C. Chappert, A. Fert, and F. N. V. Dau, The emergence of spin electronics in data storage, Nat. Mater. **6**, 813 (2007).

[2] P. J. Metaxas, J. P. Jamet, A. Mougin, M. Cormier, J. Ferré, V. Baltz, B. Rodmacq, B. Dieny, and R. L. Stamps, Creep and Flow Regimes of Magnetic Domain-Wall Motion in Ultrathin Pt/Co/Pt Films with Perpendicular Anisotropy, Phys. Rev. Lett. **99**, 217208 (2007).

[3] K.-S. Ryu, L. Thomas, S.-H. Yang, and S. S. P. Parkin, Current induced tilting of domain walls in high velocity motion along perpendicularly magnetized micron-sized Co/Ni/Co racetracks, Appl. Phys. Express **5**, 093006 (2012).

[4] S.-H. Yang, K.-S. Ryu, and S. Parkin, Domain-wall velocities of up to 750 ms^{-1} driven by exchange-coupling torque in synthetic antiferromagnets, Nat. Nanotechnol. **10**, 221 (2015).

[5] S. DuttaGupta, S. Fukami, C. Zhang, H. Sato, M. Yamanouchi, F. Matsukura, and H. Ohno, Adiabatic spin-transfer-torque-induced domain wall creep in a magnetic metal, Nat. Phys. **12**, 333 (2016).

[6] S. Emori, U. Bauer, S.-M. Ahn, E. Martinez, and G. S. D. Beach, Current-driven dynamics of chiral ferromagnetic domain walls, Nat. Mater. **12**, 611 (2013).

[7] Y. Yoshimura, K.-J. Kim, T. Taniguchi, T. Tono, K. Ueda, R. Hiramatsu, T. Moriyama, K. Yamada, Y. Nakatani, and T. Ono, Soliton-like magnetic domain wall motion induced by the interfacial Dzyaloshinskii–Moriya interaction, Nat. Phys. **12**, 157 (2016).

[8] E. De Ranieri, P. E. Roy, D. Fang, E. K. Vehsthedt, A. C. Irvine, D. Heiss, A. Casiraghi, R. P. Campion, B. L. Gallagher, T. Jungwirth, and J. Wunderlich, Piezoelectric control of the mobility of a domain wall driven by adiabatic and non-adiabatic torques, Nat. Mater. **12**, 808 (2013).

[9] H. Hopster and H. P. Oepen, SEMPA studies of thin film structures and exchange coupled layers, *Magnetic Microscopy of Nanostructures* (Springer, New York, 2005), pp. 137–167.

[10] J.-P. Tetienne, T. Hingant, J.-V. Kim, L. Herrera Diez, J.-P. Adam, K. Garcia, J.-F. Roch, S. Rohart, A. Thiaville, D. Ravelosona, and V. Jacques, Nanoscale imaging and control of domain-wall hopping with a nitrogen-vacancy center microscope, Science **344**, 1366 (2014).

[11] A. Yamaguchi, T. Ono, S. Nasu, K. Miyake, K. Mibu, and T. Shinjo, Real-Space Observation of Current-Driven Domain Wall Motion in Submicron Magnetic Wires, Phys. Rev. Lett. **92**, 077205 (2004).

[12] N. Nagaosa, J. Sinova, S. Onoda, A. H. MacDonald, and N. P. Ong, Anomalous Hall effect, Rev. Mod. Phys. **82**, 1539 (2010).

[13] J. Wunderlich, D. Ravelosona, C. Chappert, F. Cayssol, V. Mathet, J. Ferre, J. P. Jamet, and A. Thiaville, Influence of geometry on domain wall propagation in a mesoscopic wire, IEEE Trans. Mag. **37**, 2104 (2001).

[14] K. S. Novoselov, A. K. Geim, S. V. Dubonos, E. W. Hill, and I. V. Grigorieva, Subatomic movement of a domain wall in the Peierls potential, Nature (London) **426**, 812 (2003).

[15] T. Koyama, D. Chiba, K. Ueda, K. Kondou, H. Tanigawa, S. Fukami, T. Suzuki, N. Ohshima, N. Ishiwata, Y. Nakatani, K. Kobayashi, and T. Ono, Observation of the intrinsic pinning of a magnetic domain wall in a ferromagnetic nanowire, Nat. Mater. **10**, 194 (2011).

[16] C. Burrowes, A. P. Mihai, D. Ravelosona, J.-V. Kim, C. Chappert, L. Vila, A. Marty, Y. Samson, F. Garcia-Sanchez, L. D. Buda-Prejbeanu, I. Tudosa, E. E. Fullerton, and J.-P. Attané, Non-adiabatic spin-torques in narrow magnetic domain walls, Nat. Phys. **6**, 17 (2010).

[17] T. Ono, H. Miyajima, K. Shigeto, K. Mibu, N. Hosoito, and T. Shinjo, Propagation of a magnetic domain wall in a submicrometer magnetic wire, Science **284**, 468 (1999).

[18] G. E. W. Bauer, E. Saitoh, and B. J. van Wees, Spin caloritronics, Nat. Mater. **11**, 391 (2012).

[19] A. A. Kovalev and Y. Tserkovnyak, Thermoelectric spin transfer in textured magnets, Phys. Rev. B **80**, 100408(R) (2009).

[20] P. Yan, X. S. Wang, and X. R. Wang, All-Magnonic Spin-Transfer Torque and Domain Wall Propagation, Phys. Rev. Lett. **107**, 177207 (2011).

[21] D. Hinzke and U. Nowak, Domain Wall Motion by the Magnonic Spin Seebeck Effect, Phys. Rev. Lett. **107**, 027205 (2011).

[22] J. Torrejon, G. Malinowski, M. Pelloux, R. Weil, A. Thiaville, J. Curiale, D. Lacour, F. Montaigne, and M. Hehn, Unidirectional Thermal Effects in Current-Induced Domain Wall Motion, Phys. Rev. Lett. **109**, 106601 (2012).

[23] W. Jiang, P. Upadhyaya, Y. Fan, J. Zhao, M. Wang, L.-T. Chang, M. Lang, K. L. Wong, M. Lewis, Y.-T. Lin, J. Tang, S. Cherepov, X. Zhou, Y. Tserkovnyak, R. N. Schwartz, and K. L. Wang, Direct Imaging of Thermally Driven Domain Wall Motion in Magnetic Insulators, Phys. Rev. Lett. **110**, 177202 (2013).

[24] P. Krzysteczko, X. Hu, N. Liebing, S. Sievers, and H. W. Schumacher, Domain wall magneto Seebeck effect, Phys. Rev. B **92**, 140405 (2015).

[25] S. Y. Huang, W. G. Wang, S. F. Lee, J. Kwo, and C. L. Chien, Intrinsic Spin-Dependent Thermal Transport, Phys. Rev. Lett. **107**, 216604 (2011).

[26] T. Kikkawa, K. Uchida, Y. Shiomi, Z. Qiu, D. Hou, D. Tian, H. Nakayama, X.-F. Jin, and E. Saitoh, Longitudinal Spin Seebeck Effect Free from the Proximity Nernst Effect, Phys. Rev. Lett. **110**, 067207 (2013).

[27] D. Meier, D. Reinhardt, M. Schmid, C. H. Back, J.-M. Schmalhorst, T. Kuschel, and G. Reiss, Influence of heat flow directions on Nernst effects in Py/Pt bilayers, Phys. Rev. B **88**, 184425 (2013).

[28] H. Corte-León, A. Fernández Scarioni, R. Mansell, P. Krzysteczko, D. Cox, D. McGrouther, S. McVitie, R. Cowburn, H. W. Schumacher, V. Antonov, and O. Kazakova, Magnetic scanning gate microscopy of CoFeB laterl spin valve, AIP Adv. **7**, 056808 (2017).

[29] M. Mizuguchi, S. Ohata, K. Uchida, E. Saitoh, and K. Takanashi, Anomalous Nernst effect in an $L1_0$-ordered epitaxial FePt thin film, Appl. Phys. Express **5**, 093002 (2012).

[30] K. Baumgaertl, F. Heimbach, S. Maendl, D. Rueffer, A. Fontcuberta i Morral, and D. Grundler, Magnetization reversal in individual Py and CoFeB nanotubes locally probed via anisotropic magnetoresistance and anomalous Nernst effect, Appl. Phys. Lett. **108**, 132408 (2016).

[31] J. M. Bartell, D. H. Ngai, Z. Leng, and G. D. Fuchs, Towards a table-top microscope for nanoscale magnetic imaging using picosecond thermal gradients, Nat. Commun. **6**, 8460 (2015).

[32] H. Schultheiss, J. E. Pearson, S. D. Bader, and A. Hoffmann, Thermoelectric Detection of Spin Waves, Phys. Rev. Lett. **109**, 237204 (2012).

[33] See Supplemental Material at http://link.aps.org/supplemental/10.1103/PhysRevB.95.220410 for details on sample fabrication, general expression of ANE voltage for spatially varying temperature gradient, details of ANE measurements on (GaMn)(AsP) devices, information on MFM induced DW manipulation, and details on finite element simulations and thermal calibrations.

[34] R. Mansell, A. Beguivin, D. C. M. C. Petit, A. Fernández-Pacheco, J. H. Lee, and R. P. Cowburn, Controlling nucleation in perpendicularly magnetized nanowires through in-plane shape, Appl. Phys. Lett. **107**, 092405 (2015).

[35] J. M. D. Coey, *Magnetism and Magnetic Materials* (Cambridge University Press, New York, 2009).